Boosting borohydride oxidation by control lattice-strain of Ni@NiP electrocatalyst with core-shell structure

Bihao Hu [a], Yuxin Xie [a], Ying Yang [a], Jiazhi Meng [a], Jinliang Cai [a], Changguo Chen [a], Danmei Yu [a,*], Xiaoyuan Zhou [b,*]

[a] *School of Chemistry and Chemical Engineering, Chongqing University, Chongqing 401331, PR China*
[b] *College of Physics, Chongqing University, Chongqing 401331, PR China*

A B S T R A C T

Here we fabricate an efficient Ni@NiP catalyst for borohydride oxidation by simple electrodeposition, which has a core-shell structure consisting of crystalline Ni core and amorphous NiP shell. The introduction P into the shell of Ni@NiP causes the expansion of Ni lattice, raising D-band center of Ni, strengthening adsorption to reactants, and improving intrinsic activity to BOR. Ni@NiP catalyst exhibits a superior intrinsic activity of 6.3 mA $cm_{Cat.}^{-2}$ than most PGM and PGM-free catalysts. When using Ni@NiP catalyst anode, DBFC gives a peak power density of 474 mW cm^{-2}, 2.5 times higher than that with commercial Pt/C anode. Density functional theory research reveals that tensile lattice strain effectively promoted BOR activity by reducing B* intermediate formation energy on Ni@NiP surface, which is the rate-determining step in BOR and verified by electrochemical measurement results. This work brings new insights into design efficient noble-metal-free catalysts to promote practice application of DBFC technology.

1. Introduction

Although proton exchange membrane fuel cell (PEMFC) is an emerging clean energy technology, its application cost is high owing to demand a large amount of platinum group metals (PGM) catalyst [1]. Whereas the direct borohydride fuel cell (DBFC) using sodium borohydride ($NaBH_4$) as the fuel may become a cost-effective alternative of PEMFC because of its higher theoretical open-circuit voltage (OCV), higher theoretical energy density, and relatively low-cost catalysts [2–4]. When the oxidant is O_2, DBFC has a theoretical cell voltage of 1.64 V and a theoretical energy density of 9.3 kW h kg^{-1} [5], while those of PEMFCs are 1.23 V and 3.28 kW h kg^{-1}, respectively [4]. Moreover, if H_2O_2 acidic aqueous solution is used as the oxidant, the theoretical OCV reaches 2.18 V [6] and the theoretical energy density is 17 kW h kg^{-1} [7]. Given above-mentioned advantages, DBFCs has a great prospect potential application in mobile devices, submarines and space powers. However, it is a major obstacle for DBFC development to lack efficient noble-metal-free catalysts towards borohydride oxidation reaction (BOR) [8], which is the reactions on the anode.

To realize efficient DBFC, BOR catalysts are confronted with many challenges, which exhibit in not only a high intrinsic activity, but also a large surface area, a low anode potential, high fuel utilization, and resistance to the poisoning of BOR intermediates [9,10]. Currently, the best catalyst to BOR is still PGM [3,10–12], so an important goal of developing DBFC is to reduce or eliminate the need to noble metal catalysts, such as Pt, Pd, and Au [13,14]. The high catalytic activity to BOR originates from PGM having strong dissociative adsorption to borohydride, but the over-strong adsorption of Pt or Pd to borohydride also leads to accumulation of intermediate species on catalyst surface, thereby poisoning active sites and reducing catalyst stability [15,16]. In addition, due to the appropriate binding energy with hydrogen, parallel reactions such as borohydride hydrolysis and hydrogen evolution reaction (HER) can also be proceeded fast on Pt and Pd catalysts, which is going to seriously decrease the utilization rate of borohydride during fuel cell operation [17]. On the one hand, the adsorption to H atoms is so weak that the parallel side reactions of BOR carry out very slowly, leading to the emergence of an ideal 8-electron reaction on Au catalyst [9,16]. On the other hand, B-H bonds are activated and broken difficultly because the action between Au and borohydride is molecular adsorption rather than dissociative adsorption, so the catalytic activity

to BOR is very poor [18]. However, as an earth-abundant metal, Ni is a promising anode catalyst to realize the commercialization of DBFCs due to low price and aplenty reserves [9,14,19–21]. In spite of Ni exhibits stronger dissociative adsorption to borohydride among earth-abundant metals catalysts, it is still weaker than that of Pt and Pd. Although weaker dissociative adsorption makes the active sites on the Ni surface less susceptible to poison and hydrolysis [9,10], however, BOR is still an incomplete 8-electron. It is because Ni also can catalyze the borohydride hydrolysis and HER [22–25], which will reduce seriously the fuel utilization rate and bring out safety hazards during DBFC operation. Moreover, the metallic Ni exhibits high activity towards BOR, while the oxidized nickel is poor activity [9]. In other words, the catalytic performance of Ni is strongly influenced by the oxidation degree of its surface. Therefore, it is an important aspect in improving catalyst performances how to maintain the metallic state of the Ni surface.

At present, most researches still mainly focus on the composite of Ni with metals such as Pt and Pd with high activity[10,11,26–29] or Au with high selectivity[30–32] to improve their intrinsic activity and selectivity to BOR. Besides, there are also many studies on improvement performance of Ni-based catalysts by composition with non-noble metals Co[33], Zn[14], Cu[19] or non-metal elements P[20], B[33], etc. Nevertheless, up to now, the intrinsic activity of the state-of the-art Ni-based catalysts is still below 3 mA $cm_{Cat.}^{-2}$ according to literatures reported [14,17,19,21]. As a result, activity, selectivity, and stability of Ni-based catalysts should be improved urgently.

Strain engineering is considered to be an effective strategy to adjust and control the performance of catalysts [34]. The D-band center of the catalyst will be affected by the tensile or compressive lattice strain, thereby regulating the adsorption strength to reactant on catalyst surface and achieving the purpose of improvement catalytic performance [35,36]. He et al.[37] constructed a strained Pt-shell catalyst on a PdP core by phosphated/dephosphorylated and found the dependence of the lattice strain of Pt on the activities to MOR and HER. Cui et al.[38] also prepared a Pt_xNi_{1-x} alloy catalyst with a sandwich structure by electrochemical dealloying. The high compressive strain of Pt shell originates from the high Ni content in subsurface layer, so the $PtNi_3$ alloy catalyst exhibits excellent performance to ORR. However, most strain engineering strategies have been applied adjusting the performance of noble-metal-based catalysts [36–42], while the application research in the catalysts to BOR has not been reported.

Here, an efficient core-shell Ni@NiP catalyst towards BOR has been fabricated with the aid of an innovation strain engineering strategy. The core-shell structure can be formed and P element is introduced into the shell via a simple electrodeposition method. The tensile lattice strain is generated in Ni@NiP catalyst due to the introduction P and core-shell structure, which raises the d-band center of Ni and strengthens the adsorption to reactants, while the introduction P also inhibits the oxidation of Ni. Therefore, compared with Ni and Pt/C catalysts, Ni@NiP catalyst demonstrates extraordinary activity, selectivity and stability. As employing the Ni@NiP anode catalyst, DBFC delivers a peak power density of 474 mW cm^{-2} at 70 ℃, about 2.5 times higher than that of DBFC using commercial Pt/C anode under same condition. We believe that the advanced strain-engineering design idea and simple synthesis method of effective noble-metal-free electrocatalyst in this paper will push forward the practice application of DBFC technology.

2. Experiment

2.1. Materials

NiCl₂·6 H₂O, NaH₂PO₂·H₂O (NH₄)₂SO₄, C₆H₅O₇Na₃NaBH₄, H₂SO₄, and NaOH were purchased from Chengdu Cologne Chemical Co. Ltd, China. H₂O₂ and HNO₃ were purchased from Chongqing Chuandong Chemical Industry Co. LTD, China. All chemicals were used without further purification. The carbon cloth (W0S1011, thickness of

0.365 mm, air permeability of 2.3 s) was purchased from CeTech Co., Ltd.

2.2. Preparation of the Ni catalyst

The Ni catalyst was synthesized using an electrodeposition method. In this synthesis, the traditional three-electrode system was used for electrodeposition. The pretreated carbon cloth with an area of 1 cm^2 was the working electrode (WE), the carbon strip was the counter electrode (CE), the saturated calomel electrode (SCE) was the reference electrode (RE), and the mixed solution of 1 M NiCl₂·6 H₂O and 0.1 M (NH₄)₂SO₄ was deposition solution. Before deposition, carbon cloth was thoroughly rinsed with ultrasonic in absolute ethyl alcohol and deionized water for 5 min, respectively, and then soaked in a concentrated HNO₃ solution for 5 min to improve hydrophilicity, at final, thoroughly rinsed again with ultrasonic in deionized water to remove residues. A three-step electrodeposition procedure with E_1 = - 0.8 V (10 s), E_2 = - 2.4 V (15 s), and E_3 = - 1.8 V versus sSCE (210 s) was applied to prepare the Ni catalyst using electrochemical station (CHI 660e, Shanghai Chen Hua Instrument Co. Ltd.). Finally, the Ni catalyst was rinsed thoroughly with deionized water for standby.

2.3. Preparation of the Ni@NiP catalysts

The preparation of Ni@NiP catalysts can be divided into two steps: the oxidation of pre-prepared Ni catalyst and the subsequent Ni and P co-deposition to form the shell.

Oxidation of pre-prepared Ni catalyst is to obtain a smaller Ni core for deposition of NiP shell, to avoid the significant variation of the surface area and increase of Ni loading amount after NiP deposition on it for better comparison. The pre-prepared Ni catalyst, carbon strip, and SCE were used as the WE, the CE, and the RE, respectively, and the mixed solution of 0.2 M NiCl₂·6 H₂O, 0.25 M (NH₄)₂SO₄, 0.1 M C₆H₅O₇Na₃, and 1.2 M NaH₂PO₂·H₂O was the deposition solution, in order to assemble into a three-electrode system. A constant potential of 0.6 V was applied to the WE for 111 s by the electrochemical station. The oxidized Ni catalyst was denoted as Ni-ox.

Deposition of NiP shell was carried out in the same three-electrode system except that the WE used the Ni-ox. A constant potential of - 1.2 V was applied to the WE for 76 s by the electrochemical station. Then the deposited electrode was washed thoroughly with deionized water for standby. Catalysts were also prepared in the deposition solution with different NaH₂PO₂ concentrations. The prepared catalysts were donated as Ni@NiP-x, where x represents the NaH₂PO₂ concentration (M) in the deposition solution. The preparation process of Ni and Ni@NiP catalysts is illustrated in Fig. S1.

2.4. Materials characterizations

The morphology and structure of prepared catalysts were measured by a field emission scanning electron microscope (FE-SEM, Quattro S) and transmission electron microscopy (TEM, Talos F200S). The lattice strain of prepared samples was calculated by Eq. (1):

$$\text{Lattice } strain = |a_{\text{strained}} - a_0| \, / \, a_0 \times 100\% \qquad (1)$$

Where a_{strained} is the measured lattice spacing of Ni (111) crystal facet of prepared catalysts and a_0 is the standard lattice spacing of Ni (111) crystal facet.

X-ray diffraction (XRD) patterns of prepared catalysts were recorded by a Rigaku D/MAX2500PC with Cu Kα radiation at 40 kV and 40 mA. In XRD measurement, catalyst samples were prepared by tablet pressing method. Specifically, the prepared catalyst was ground thoroughly in an agate mortar to obtain fine powder, then added to the middle of the groove in sample holder and gently pressed the powder surface with a glass slide to get a uniform flat surface and flush with the groove plane. Rietveld refinements were performed by GSAS using a P-V/FCJ Asym

peak profile function. The lattice parameter and microstrain (ε_{micro}) are obtained from the Rietveld refinement results by GSAS. Dispersion factor (D) was introduced to represent the surface atom ratio in order to calculate the surface area normalized microstrain (SA-ε_{micro}). D can be calculated by the Eq. (2) and the model proposed by Montejano-Carrizalles et al.[43,44].

$$D = \frac{N_s}{N} \tag{2}$$

Where N and N_s are the total number of atoms and the number of surface atoms, respectively, and can be calculated by the Eqs. (3) and (4):

$$N = 10\frac{m^3}{3} + 5m^2 + \frac{11}{3}m + 1 \tag{3}$$

$$N_s = 10m^2 + 2 \tag{4}$$

m represents the atomic layers number of crystallite in the Montejano-Carrizales model. The values of m can be obtained by the Eq. (5):

$$m = \frac{d}{2\sqrt{3}r_{Ni}} \tag{5}$$

Here d is the crystallite size, which can be obtained from the refinement data, and r_{Ni} is the atomic radius of Ni (0.124 nm).

The X-ray photoelectron spectroscopy (XPS, Thermo Fisher Scientific ESCALAB250Xi, Al Kα) was performed to explore the surface composition of prepared catalysts, where the C 1 s peak at 284.8 eV (i.e. the surface adventitious carbon) was used to be as the calibration peak.

2.5. Electrochemical measurements

All electrochemical measurements were performed in a standard three-electrode system controlled by an electrochemical station (CHI 660e/760e, Shanghai Chen Hua Instrument Co. Ltd.). The prepared catalyst was used as the WE, a mercury/mercury oxide (Hg/HgO) electrode was used as the RE ($E_{Hg/HgO} = 0.924$ V vs. reversible hydrogen electrode (RHE), pH = 14.3), and carbon strip was used as the CE. All the potential values in the paper were defined versus RHE. The electrochemically active surface areas (ECSA) of all prepared catalysts were calculated according to Eq. (6).

$$ECSA = \frac{C_Q}{C_s} \tag{6}$$

Where C_Q is the charge of desorption of hydroxyl species, which was measured by the cyclic voltammetry (CV) performed in 0.1 M KOH solution at a scan rate of 50 mV s^{-1} [45–47]. C_s is theoretical specific capacitance of Ni catalyst in alkaline electrolyte (514 μC cm^{-2}).

For performance measurements of BOR, the Ni or Ni@NiP catalyst was used as the WE and the mixed solution of 0.15 M NaBH$_4$ and 2 M NaOH was used as the electrolyte. CV test of BOR was carried out with open-circuit potential (OCP) as initial potential, low potential and end potential, 0.3 V as high potential at a scan rate of 10 mV s^{-1} and 298 K. Prior to the test, CV tests of BOR on prepared catalysts were scanned rapidly at a scan rate of 100 mV s^{-1} for 10 cycles to remove impurities on its surface, which may contribute current. Chronoamperometry (CA) tests were conducted at 0.2 V. Electrochemical impedance spectroscopy (EIS) was performed in the range of 10^{-2} Hz $\sim$ 100 kHz with a signal amplitude of 5 mV around $E = 0.1$ V. The values of circuit elements were simulated according to the equivalent circuit via ZSimpWin. The values of activation energies (E_a) of BOR on prepared catalysts were evaluated by CV test at different temperatures according to the Arrhenius Eq. (7) [48]:

$$\frac{\partial \ln j}{\partial \frac{1}{T}} = -\frac{E_a}{R} \tag{7}$$

Where j (mA cm^{-2}) is the current density at 0.3 V recorded on CV curves, T (K) is the test temperature, E_a (J mol^{-1}) is the activation energy, and R is the gas constant (8.314 J mol^{-1} K^{-1}). Fuel efficiency was obtained from chronopotentiometry using the LAND system at a constant current of 20 mA. The transfer electron number of BOR on prepared catalyst was evaluated through CV curve test at different rotating speeds in a mixed solution of 5 mM NaBH$_4$ and 1 M NaOH. The prepared catalyst was cut into a size of 2 mm × 2 mm and then fixed carefully by cotton thread on a glassy carbon rotating disk electrode (RDE, Ø = 5 mm, Tianjin Aida Hengsheng Technology Development Co., Ltd.), which was used as the WE in a three-electrode system. The starting potential, stopping potential, and low potential were - 0.2 V, while the high potential was 0.3 V, and the scan rate was 20 mV s^{-1}. The rotating speed of the WE is 0, 100, 200, 400, 600, and 900 rpm. The transfer electron number of electrode reaction can be calculated according to the Koutecky-Levich Eq. (8):

$$j^{-1} = j_k^{-1} + j_d^{-1} = j_k^{-1} + B^{-1}\omega^{-0.5} \tag{8}$$

Where j_k^{-1} is a dynamic current density, j_d^{-1} is the limiting diffusion current density, and ω is the rotating speed. B can be calculated according to Levich Eq. (9):

$$B = 0.62nD^{2/3}F\nu^{-1/6}c_0 \tag{9}$$

Where n is the transfer electron number, D is the diffusion coefficient of borohydride (2.6 × 10^{-5} cm^2 s^{-1})[49], F is Faraday constant (96, 485 C mol^{-1}), ν is the dynamic viscosity of electrolyte (0.0118 cm^2 s^{-1}) [49], and c_0 is the concentration of NaBH$_4$.

For performance measurements of HER, the catalytic activity tests were carried out in 2 M NaOH solution by liner sweeping in the range of about - 0.1 $\sim$ 0.4 V at a scan rate of 10 mV s^{-1} and 298 K.

2.6. Fuel cell study

The unit DBFC was composed of a polyester box, metal plate, insulating sheet, current collector, graphite flow cell, sealing ring, anode catalyst, cathode catalyst, and a membrane with an active surface area of 5 cm^2, in which the carbon cloth is compressed by 45 %, as shown in Fig. S2. Anodic and cathodic flow fields are single-serpentine channels. The Ni@NiP catalyst, commercial Pt/C catalyst (Johnson Matthey, 1 mg cm^{-2}) and commercial Pd/C catalyst (Suzhou Sinero Technology Co., Ltd, 1 mg cm^{-2}) was employed as the anode, respectively, and all the cathodes were the commercial Pt/C catalyst. To fabricate Pt/C and Pd/C catalyst, 5 mg of Pt/C or Pd/C, 180 μL absolute ethanol, and 20 μL 5 % Nafion solution (binder) were mixed by ultrasonic for 5 min to obtain a black ink. The ink was evenly dropped on a 5 cm^2 carbon cloth and then dried in room temperature. Nafion® 117 (183 μm) was used as a separator to ensure ion transport between the anode and cathode, and avoid direct contact between the anolyte and catholyte. The mixed solution of 1.5 M NaBH$_4$ and 3 M NaOH, and mixed solution of 1.5 M H$_2$O$_2$ and 2 M H$_2$SO$_4$ were used as the anolyte and catholyte, respectively. The fuel flowrate was optimized as it can mitigate parasitic reactions and lessens anode passivation by hydrogen bubbles. According to Fig. S3, the optimal flowrate of 15 mL min^{-1} cm^{-2} was chosen for DBFC performance test. Neware battery test system (CT-4008–5V6A-S1) was used to obtain polarization curves ($I \sim E$) by scanning the current from 0.1 mA cm^{-2} to 400 mA cm^{-2} by holding 1 min at each current density at 70 °C.

2.7. Density functional theory calculations

All theoretical calculations in this paper were based on Density Functional Theory (DFT), and the model structure optimization and the calculation of related properties were performed by the Vienna Ab Initio Simulation Package program [50]. While the generalized gradient approximation (GGA)[51] modified Per-dew-Burke-Ernzerhof method

[52,53] was used to describe the exchange-association function. The interaction between particles in the system was described by the Projector Augmented Wave (PAW) pseudopotential method [54]. The cut-off energy of the plane wave basis set was selected as 450 eV, and the size of the k point in the Brillouin zone was generated by the Monkhorst-Pack lattice method [55]. The k-point size was set to $3 \times 3 \times 1$ and $5 \times 5 \times 2$ for the calculation of the unit cell optimization and related properties, respectively. In order to obtain accurate results, the convergence criteria were set as the interatomic interaction force is less than 0.010 eV Å^{-1} and the energy change of the whole system was less than 1×10^{-5} eV per atom. Ni (111) which was composed of 4 layers of 2×2 supercells containing 64 Ni atoms, was used to construct the surface. The two layers in the bottom were confined to the lattice sites of the face-centered cubic stacking of Ni, while the two layers in top layers were allowed to relax. A tensile lattice strain parallel to the surface was applied to the catalyst by adjusting the lattice constant of the unstrained Ni (111) crystal facet, and the value of tensile lattice strain was determined from the TEM results. Interactions between periodic surfaces are minimized by establishing a vacuum layer of 15 Å in the z direction.

3. Results and discussion

3.1. Characterization of the strained Ni@NiP

The morphology of prepared samples can be characterized by scanning electron microscope (SEM). Fig. 1a shows the morphology of the Ni catalyst at the first deposition, which is consist of dispersed popcorn-like microspheres with a size of $1 \sim 2$ μm on the carbon cloth fibers. From Fig. 1b, it can be seen that the size of these nickel microspheres is significantly reduced to 500 nm after anodization. The popcorn-like

microsphere morphology of prepared catalyst is still maintained after the Ni P co-deposition according to our established procedure[56], shown as Fig. 1c. Fig. S4 shows that the Ni element is uniformly distributed in whole prepared catalyst, while P is mainly distributed in the microsphere region. This indicates that the prepared catalyst is composed of Ni and P elements, while the P element may exist only on the surface of microspheres, implying that it may possess a structure of NiP shell and Ni core. The microstructure of prepared catalyst can be further characterized by transmission electron microscopy (TEM), and the similar popcorn-like microsphere morphology is also observed in Fig. 1d. From the high-resolution TEM (HR-TEM) images in Fig. 1e, clear lattice fringes can be seen on the right of the orange line, which belong to the (111) crystal facet of face center cubic Ni. While no lattice fringes are found on the left of the orange line, corresponding to amorphous NiP. In addition, it can also be seen in Fig. S5 that there are distinct interfaces between crystalline Ni and amorphous NiP. Fig. 1f and g show separately the fast Fourier transform (FFT) images of the selected dashed line area from Fig. 1e. The bright spots found in Fig. 1f correspond to (111) facet of Ni crystal, indicating existence of crystalline core. While the absence of bright spots in Fig. 1g confirms the formation of amorphous shell. The element mapping image in Fig. 1h shows that Ni is distributed mostly in the inner while P is scattered in the outer. In summary, it may confirm that the prepared catalyst has a unique structure of amorphous NiP shell and crystalline Ni core, denoted by Ni@NiP.

Furthermore, based on above analysis results, the formation process of Ni@NiP catalyst may be illustrated by Fig. 1i. During the first deposition, Ni^{2+} is reduced to Ni and deposited on the surface of the carbon cloth fiber to form popcorn-like Ni microspheres. Then followed an anodization, the partial deposited nickel is oxidized to Ni^{2+} and dissolved in the deposition solution, so the size of Ni microspheres is
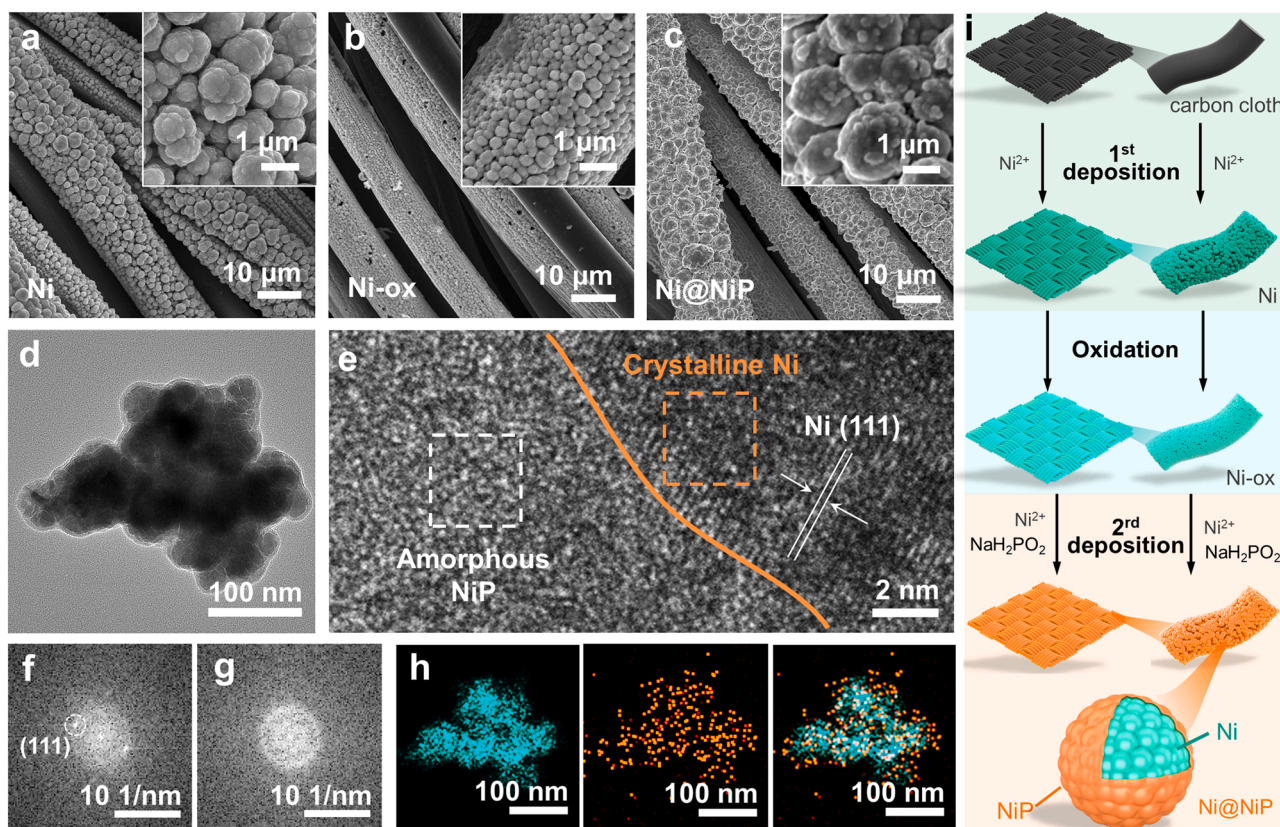

Fig. 1. (a-c) SEM images of the Ni, Ni-ox, and Ni@NiP, respectively; (d) TEM and (e) HR-TEM images of the Ni@NiP; FFT images of (f) orange and (g) white dotted area in Fig. (e); (h) elemental mapping images of the Ni@NiP in Fig. (d) (cyan and orange dots represent Ni and P elements, respectively); (i) the schematic diagram of the formation process of the Ni@NiP.

reduced. When it comes to the second deposition, Ni and P are co-deposited on the surface of Ni microspheres with the help of trisodium citrate to form an amorphous NiP alloy shell.[56] Besides, the P content of Ni@NiP varies with the NaH_2PO_2 concentration in deposition solution (Fig. S6). Higher concentration of NaH_2PO_2 is in the deposition solution, the higher atomic ratio of P introduces into the NiP shell. All Ni@NiP-x (x represents the NaH_2PO_2 concentration in deposition solution (M)) samples show similar popcorn-like morphologies, suggesting

that the P content affects hardly on its morphology.

To comfirm the existence of the lattice strain in the Ni@NiP, the lattice spacings of Ni core in different areas are measured. In Fig. 2a, selected three areas according to the distance from the amorphous NiP shell are respectively represented as area 1 the orange box, area 2 the cyan box, and area 3 the grey box. According to Fig. 2(b), the lattice spacing of Ni (111) in area 1 is 2.09 Å with a tensile lattice strain of 3%. This is attributed to the lattice expansion originating from the
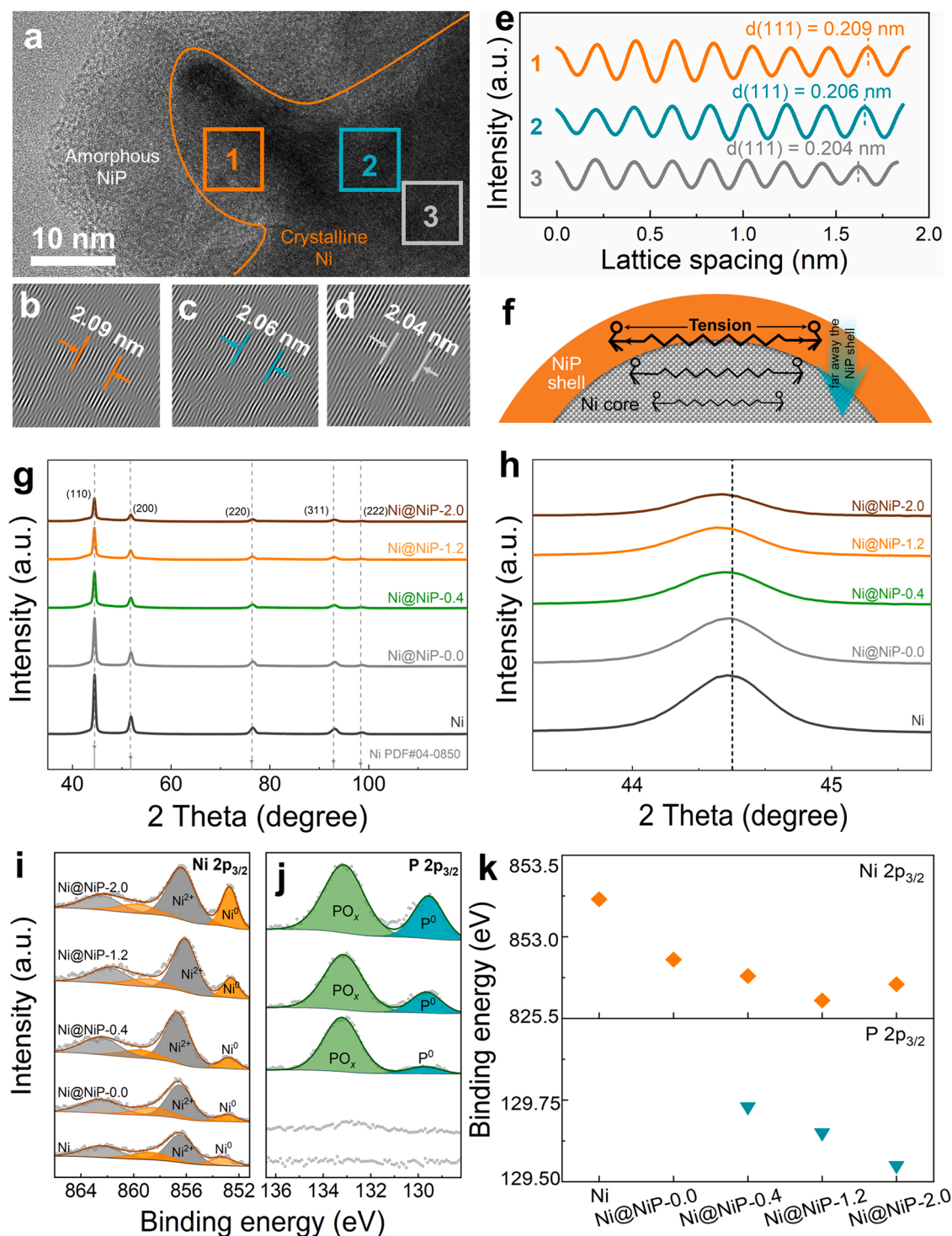
Fig. 2. (a) HR-TEM image of the Ni@NiP-1.2; (b-d) processed lattice fringe images of areas 1, 2, and 3 in Fig. (a), respectively; (e) light intensity profiles of lattice fringe images in Fig. (b-d); (f) schematic illustration of the tensile lattice strain in the Ni@NiP; (g) XRD patterns and (h) enlarged views of diffraction peaks of (111) crystal facet of the Ni and Ni@NiP-x; (i) spectrums of Ni $2p_{3/2}$, (j) spectrums of P $2p_{3/2}$, and (k) the change of binding energy of Ni^0 and P^0 in the Ni and Ni@NiP-x.

introduction of P [57], resulting in the lattice mismatch between the Ni core and NiP shell, as well as the lattice tension of Ni core. From Fig. 2 (b-e), the intensity profiles of the Ni lattices show a gradual negative shift with the increases distance from the NiP shell, indicating the enlargement of lattice spacing of Ni. The lattice spacings of Ni (111) in area 1, 2 and 3 are 2.09 Å, 2.06 Å and 2.04 Å, corresponding to tensile lattice strain of 3%, 1.5%, and 0.5%, respectively. This demonstrates that the effect of shell expansion on the lattice spacings of the Ni core gradually is weakened with the increase distance from the NiP shell illustrated as Fig. 2f, which is also confirmed in Fig. S7. The changes of Ni lattice constants can be also characterized by powder X-ray diffraction (XRD). Fig. 2g shows that all prepared catalysts have similar XRD patterns, with diffraction peaks located at 44.5°, 51.8°, 76.4°, 92.9°, and 98.4°, corresponding to (111), (200), (220), (311), and (222) crystal facets of Ni (PDF #04–0850), respectively. So, this indicates that all prepared catalysts have crystalline structure of face-centered cubic. From Fig. 2h, it can be seen that the diffraction peaks of (111) shift

negatively gradually with the increase of P content in Ni@NiP-x, confirming that the introduction of P make expand the Ni lattice as well. The XRD refinement data in Table S1 reveals that the lattice constant of Ni@NiP-x increases with the increase of P content, which suggests that the more P is introduced into the shell, the greater tensile lattice strain prepared catalysts is. This also further confirms, with our strategy, tensile lattice strain can be generated successfully in the Ni@NiP.

The impact of the tensile lattice stain on the surface electronic structure of Ni is evaluated by X-ray photoelectron spectroscopy (XPS), shown as Fig. 2i and j. The peaks near 853.0 eV and 858.5 eV corresponded to the metallic Ni (Ni^0) and its satellite peaks,[58] while the peaks near 856.5 eV and 862.0 eV are attributed to Ni^{2+} and its satellite peaks.[59] Moreover, the P^0 and PO_x peaks in Ni@NiP are located around 129.6 eV and 133.0 eV, respectively.[60] From Fig. 2k, it can be found that the binding energy of Ni^0 reduces due to strain generation and further decreases with the increase of P content in Ni@NiP-x, implying that tensile lattice strain may originate from the introduction
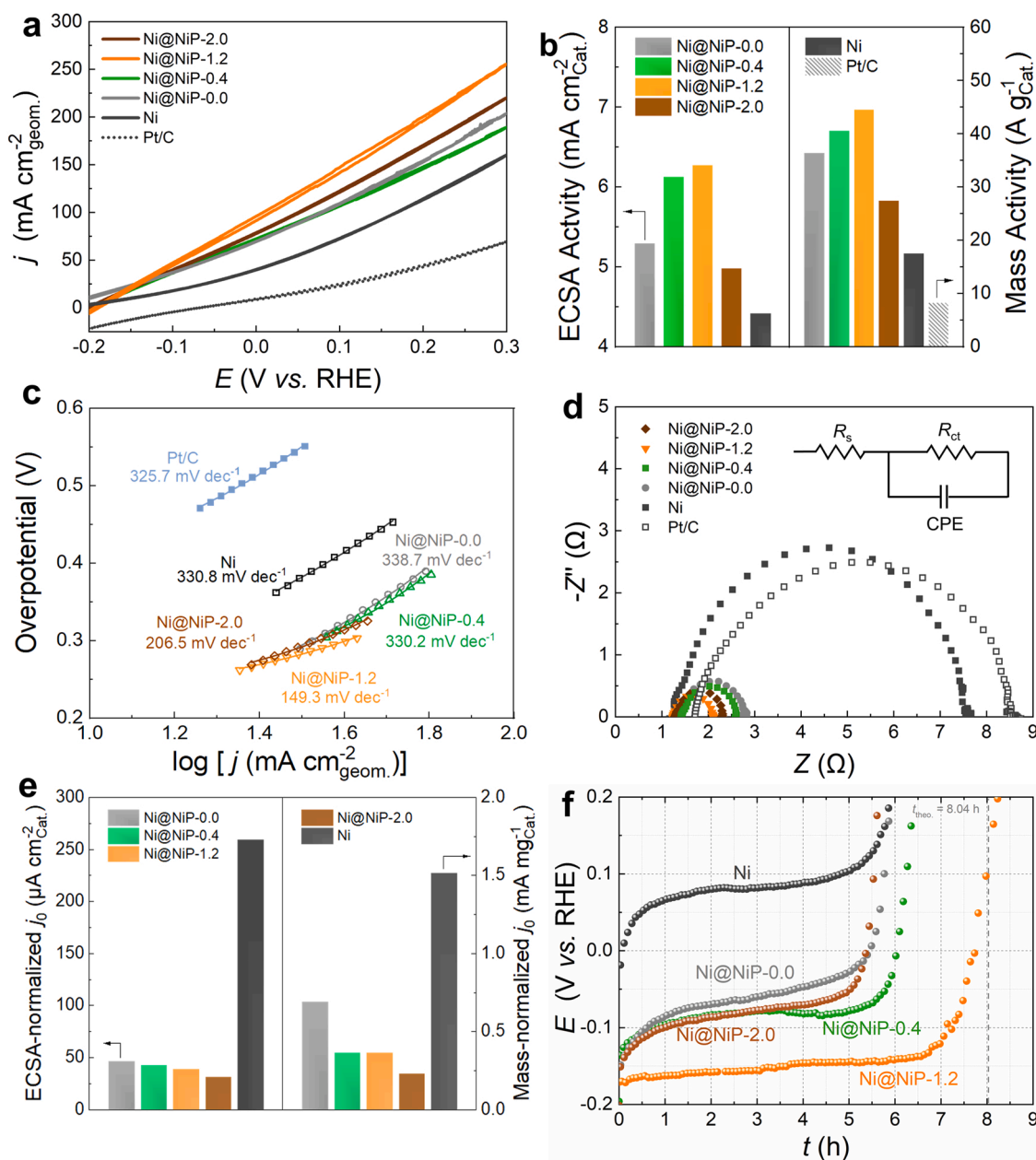
Fig. 3. (a) CV curves, (b) ECSA and mass normalized activities, (c) Tafel curves, and (d) EIS of BOR on the Ni@NiP-x, Ni, and Pt/C; (e) ECSA and mass normalized j_0 of HER on the Ni@NiP-x and Ni; (f) discharge curves of BH_4^- on the Ni and Ni@NiP-x.

P into shell. This can be attributed to tensile lattice strain increases the distance between adjacent Ni atoms. While the larger distance causes the decease in the degree of electron cloud and D-band overlap between adjacent Ni atoms[34]. And lower electron cloud density of Ni nucleus outside results in the decrease binding energy of Ni^0. According to D-band theory, the decreased D-band overlap will shift positively the D-band center of Ni, which leads to enhanced adsorption strength to reactants.[61] However, excessive P leads to the binding energy decrease of Ni^0 (Ni@NiP-2.0). This is because the electrons of Ni atoms shift more to P atoms with phosphorus content increase of Ni@NiP-x due to greater electronegativity of P than that of Ni, resulting in raise binding energy of Ni^0. The tunable electronic structure is expected to realize the adjustable adsorption of chemical species to the metal surface[42,61]. Hence, it should be possible to optimize the lattice strain of Ni@NiP-x by changing P introduction content into the shell, thereby realizing the control of reactant adsorption and promoting BOR. Multiple structural defects in the core-shell structure can also impact electronic structure and catalytic performance[34,62–64], which can be described as microstrain (ε_{micro}) and surface area normalized microstrain (SA-ε_{micro}). According to Table S1, the ε_{micro} and SA-ε_{micro} of each catalyst are negligible (much less than 0.3%), indicating that the impact of multiple structural defects on Ni@NiP-x can be excluded. In addition, the increase of Ni^0 peak area with the addition of P content in the Ni@NiP-x demonstrates that the introduction of P into the shell is beneficial to inhibiting Ni oxidation and maintaining its metallicity[60].

3.2. Catalytic performance to BOR

Electrochemical measurements were performed to evaluate the activity of prepared catalysts to BOR. As shown in Fig. 3a, the current densities of BOR on the Ni@NiP-x are higher than those on the Ni and Pt/C, indicating excellent catalytic activity to BOR. Among them, the highest current density of BOR on the Ni@NiP-1.2 reaches 255 mA cm^{-2} at 0.3 V . To explore whether the improvement of Ni@NiP-x catalytic activity originates from the catalytic sites number, the ECSAs of all catalyst were measured and shown in Fig. S8. According to Fig. S8f, the ECSA of Ni@NiP-1.2 with the highest catalytic activity is not the largest, only 40 cm^2, which is slightly higher than that of Ni (36 cm^2). Therefore, it can confirm that the significantly enhanced catalytic activity of Ni@NiP-1.2 should be attributed to the improvement of its intrinsic catalytic activity, but not the increase in the number of catalytic sites number. The intrinsic catalytic activity may be strongly impacted by the tensile lattice strain because it can adjust the adsorption to reactants and optimize the catalytic activity[37]. The ECSA and mass activities to BOR of all prepared catalysts are compared in Fig. 3b. It can also be found that on Ni@NiP-x catalyst, the ECSA and mass activities to BOR show a trend of first increase and then decrease with P content addition, indicating the lattice tension can boost the intrinsic catalytic activity towards BOR. Yet excessive strain will reduce intrinsic catalytic activity. ECSA and mass activities of Ni@NiP-1.2 are as high as 6.3 mA cm$^{-2}_{Cat.}$ and 44.6 A g$^{-1}_{Cat.}$ at 0.3 V , about 1.5–2.5 times than those on Ni catalyst, exhibiting the best catalytic activity. Multiple structural defects routinely occurred in the core-shell structure may act as highly active sites to dominate activity, but results of XRD refinement have indicated that the ε_{micro} and SA-ε_{micro} are rather small and little difference across samples (Table S1). Therefore, this influence on the activity of catalysts may be negligible. Moreover, from what we know so far, Ni@NiP-1.2 delivers the highest intrinsic catalytic activity to BOR among the metal-based catalysts as shown in Table S2. Tafel slopes were obtained to further evaluate the activity of catalysts to BOR. The Tafel slopes on Ni@NiP-x are lower than that on Ni, indicating faster kinetics of BOR (Fig. 3c). On Ni@NiP-1.2, the lowest Tafel slope of 149.3 mV dec^{-1} is gained, which is dramatically lower than the corresponding values on Ni (330.8 mV dec^{-1}) and Pt/C (325.7 mV dec^{-1}). Electrochemical impedance spectroscopy (EIS) Nyquist plots were fitted based on the

equivalent circuit as the inset in Fig. 3d. R_s, R_{ct}, and C_{dl} represent separately solution resistance, charge mass transfer resistance, and electric double-layer capacitance. The fitted R_{ct} values of Pt/C, Ni, Ni@NiP-0.0, Ni@NiP-0.4, Ni@NiP-1.2, and Ni@NiP-2.0 are 5.48, 6.10, 1.35, 1.44, 0.76, and 0.97 Ω, respectively. On the Ni@NiP-x, R_{ct} values are much smaller than those on Ni and Pt/C, which is beneficial to BOR, and the smallest R_{ct} value appears on Ni@NiP-1.2. The double-layer capacitance (C_{dl}) of different Ni-based catalysts was calculated from EIS data in Table S3. The slightly different values of C_{dl} for all prepared catalysts confirm their similar ECSA. According to the chronoamperometry (CA) curves in Fig. S9, under the same conditions, the current density of BOR on Ni@NiP-x is higher than that on Ni and Pt/C. It can confirm Ni@NiP-1.2 has the highest catalytic activity because the largest current density of BOR is obtained on it, which is consistent with the test results of the cyclic voltammetry (CV).

The catalytic activity to HER, a competing reaction for BOR, was also researched. From Fig. 3e, it can be found that on the Ni@NiP-x, the ECSA-normalized and mass-normalized exchange current densities (j_0) of HER decrease with the increase of P content. At the same time, Tafel slope also increases and j_0 decreases with increase of P content as in Fig. S10. In the view of research results above, it can conclude that the tensile lattice strain, on the one hand, may enhance the catalytic activity of Ni towards BOR, on the other hand, inhibit the catalytic ability towards HER, thereby improving the selectivity of Ni@NiP-x. Furthermore, Fig. 3f exhibits the discharge curves of BOR on different catalysts. On the Ni@NiP-1.2, the discharge platform is the most negative, around - 0.15 V , while the most positive discharge platform is observed on the Ni, at 0.1 V . This could ascribe to the highest activity to BOR and poor activity to HER on Ni@NiP-1.2, resulting in that the same current can be obtained at the lowest potential. Moreover, the more negative discharge potential could be beneficial to provide a higher OCV for DBFC. From Fig. 3f, on all Ni@NiP-x, the discharge time of BOR is longer than that on the Ni. Notably, the longest discharge time obtained on the Ni@Ni-1.2 is nearly twice that on the Ni and close to the theoretical discharge time [4]. Additionally, the discharge of BOR on the Ni@NiP-1.2 can proceed stably for 7 h on the Ni@NiP-1.2 until reactants depletion, suggesting outstanding stability. Besides, it can be found from Fig. S11 that the current decay rates on the Ni@NiP-x are smaller than those on the Ni and Pt/C, indicating further excellent stability. Of course, it may demonstrate that the construction of a NiP shell on the Ni core can enhance the stability of Ni because the oxidation passivation of metallic Ni is inhibited due to the introduction P according to the XPS results. In a word, the catalytic activity, stability, and selectivity of Ni@NiP are effectively improved by tensile lattice strain owing to the unique core-shell structure, which consists of crystalline Ni core and amorphous NiP shell.
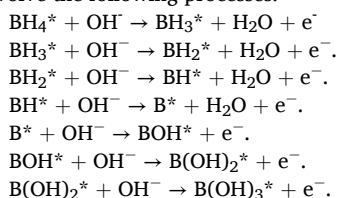
3.3. Preliminary exploration of catalytic mechanism

The above analysis and discussion indicate that the catalytic performances of Ni@NiP are strongly impacted by minor strain variations. For further insight into the performance improvement on Ni@NiP-x, the activation energy (E_a) of BOR on prepared catalysts was evaluated by the CV test as shown in Fig. S12. From Fig. 4a, the E_a on all Ni@NiP-x are lower than that on the Ni. And the lowest E_a is obtained on Ni@NiP-1.2, namely 8.1 kJ mol^{-1}, implying the highest catalytic activity to BOR. The transfer electron number of BOR was measured. The CV tests of the BOR on prepared catalysts were carried out at different rotating rates (Fig. S13). Fig. 4b displays, on different catalysts, the transfer electron number of BOR at various potential. It can be seen that no matter how high the potential is, transfer electron numbers on Ni and Ni@NiP-0.0 catalysts are close to 3, suggesting that the fourth-electron step of BOR, which is the formation of B* intermediate, is hardly processed on unstrained Ni-based catalysts. This also implies that the formation of B* intermediate might be the rate-determining step (RDS). However, on Ni@NiP-0.4, Ni@NiP-1.2, and Ni@NiP-2.0, which possess a NiP shell,
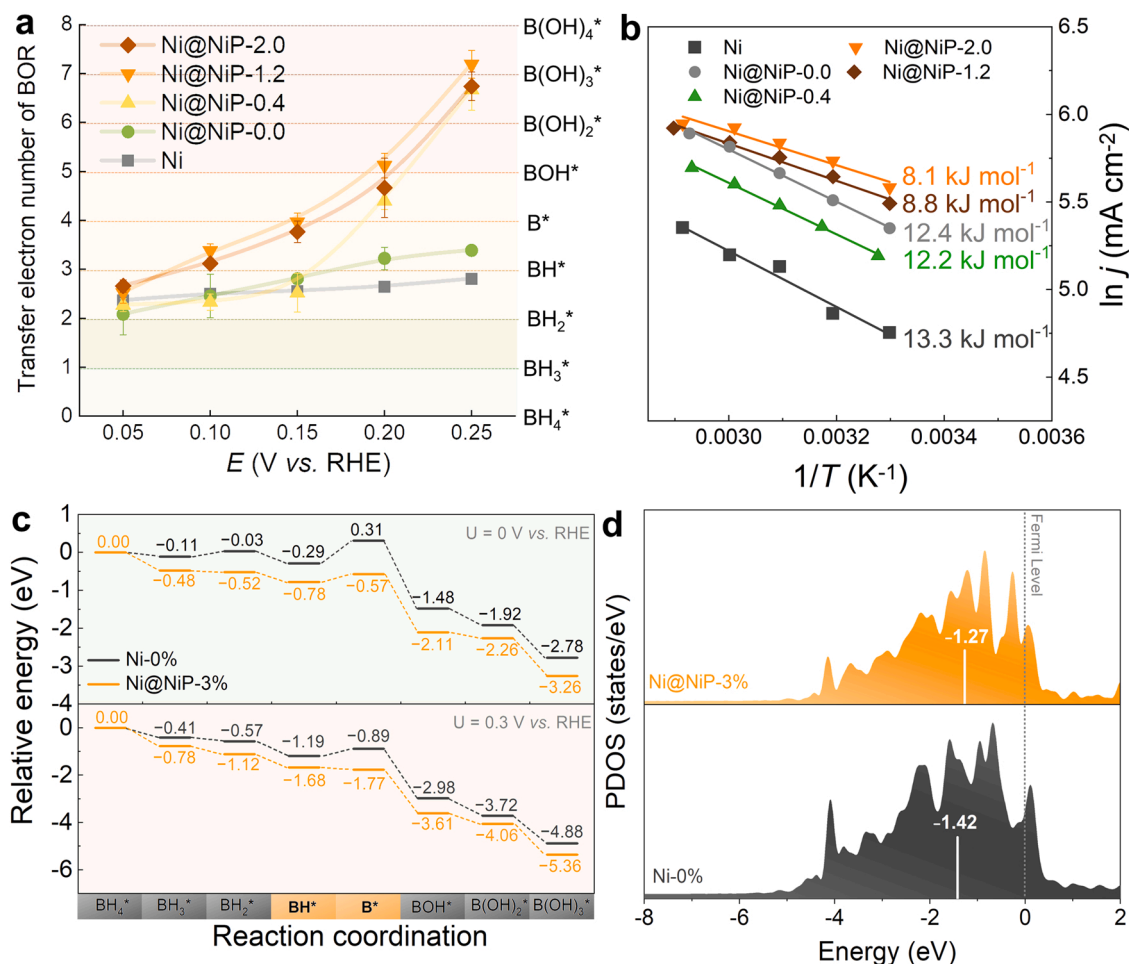
Fig. 4. (a) Transfer electron number of BOR on the Ni@NiP and Ni at various potentials; (b) ln$j$ ~ 1/T relation of BOR on Ni@NiP and Ni catalyst electrodes at 0.25 V; (c) energy profiles of BOR on the Ni@NiP-3% and Ni-0% surface at U = 0 V and 0.3 V ; (d) DOS of the Ni 3d band in Ni@NiP-3 % and Ni-0 %.

the transfer electron numbers increase with the oxidation potential raising. On Ni@NiP-0.4, Ni@NiP-1.2, and Ni@NiP-2.0 the transfer electron number at 0.15 is around 4 and further increases to 6 ~ 7 at 0.25 V . More than 4 of transfer electron number of BOR on these strained Ni@NiP catalysts means that the energy required for the RDS is reduced due to the introduction of P, which is accord with the result of E_a measurement. Notably, on the Ni@NiP-1.2, the transfer electron number of BOR is the highest, which is 7.2 at 0.25 V . It can be attributed to the lowest E_a on Ni@NiP-1.2, which indicates the borohydride is most easily oxidized to release more electrons. This also rationalizes why its catalytic activity and selectivity towards BOR are excellent. Combining above analysis and literature[65], the BOR on the Ni@NiP-1.2 may involve the following processes:

$BH_4^* + OH^- \rightarrow BH_3^* + H_2O + e^-$
$BH_3^* + OH^- \rightarrow BH_2^* + H_2O + e^-$.
$BH_2^* + OH^- \rightarrow BH^* + H_2O + e^-$.
$BH^* + OH^- \rightarrow B^* + H_2O + e^-$.
$B^* + OH^- \rightarrow BOH^* + e^-$.
$BOH^* + OH^- \rightarrow B(OH)_2^* + e^-$.
$B(OH)_2^* + OH^- \rightarrow B(OH)_3^* + e^-$.

In order to reveal further the reason behind the significantly enhanced activity of BOR on the Ni@NiP, Density Functional Theory (DFT) was performed. Two catalyst models were established, which are Ni@NiP with 3 % tensile lattice strain, donated as Ni@NiP-3 %, and the Ni without tensile lattice strain, donated as Ni-0 %, as shown in Fig. S14. Fig. 4c shows the energy profiles of borohydride oxidation at 0 V and 0.3 V , respectively, and the corresponding structures of reaction

intermediates of BOR on Ni@NiP-3 % and Ni-0 % surface are separately displayed in Fig. S15 and S16. Each step in the reaction energy profiles represents one-electron oxidation elementary reaction, where the proton electron pairs generated or water molecules are not shown. At 0 V and 0.3 V , only the reaction from BH* to B* is uphill according to Fig. 4c, which is an energetically unfavorable endothermic reaction. So, it can be confirmed that the formation of B* intermediate is RDS of BOR, consistent with the research result of transfer electron number. However, the energy difference of the RDS is reduced significantly due to the tensile lattice strain appearance under the same conditions. Moreover, for Ni@NiP-3 % at 0.3 V , all elementary steps of BOR, from BH₄* to the final B(OH)₃*, are energetically favorable downhill (exothermic). This demonstrates that the B* intermediate is much more active on Ni@NiP-3 % than on Ni-0%, thus, it can be said that the catalytic activity to BOR is remarkably improved by the tensile lattice strain originating from the introduction P and core shell structure. And it has also been confirmed by the electrochemical measurement result. In addition, the mechanism of borohydride hydrolysis reaction, a major side reaction in BOR, is also explored to reveal the effect of tensile lattice strain on the catalytic selectivity of Ni-based catalyst. According to a four-step borohydride hydrolysis mechanism [66–68], optimized structures of corresponding intermediates on Ni-0% and Ni@NiP-3% surface are shown in Fig. S17 and S18. From Fig. S19, the first two steps are the energetically unfavorable uphill processes, especially the highly endothermic reaction of $BH_2(OH)_2$ formation. Notably, the reaction energies of $BH_3(OH)$ and $BH_2(OH)_2$ formation on the Ni@NiP-3 % surface are significantly higher than those on Ni-0 % surface, indicating that the Ni@NiP-3% surface is

less preferable for borohydride hydrolysis, suggesting its higher selectivity to BOR.

Density of states (DOS) calculation and analysis are also good means to further explore the reasons for the significantly improved catalytic activity of Ni@NiP to BOR and the effect of tensile lattice strain on the electronic structure of the catalyst. For the Ni@NiP-3 %, the DOS at the Fermi level is mainly contributed by Ni while the electron density of P is almost zero as shown in Fig. S20, suggesting that Ni is the catalytic active center. From Fig. 4d, the D-band center of Ni@NiP-3 % is − 1.27 eV higher than that of Ni-0 % (− 1.42 eV). However, this positive shift may be originated from the tensile lattice strain or P-introducing. To understand the effect of tensile lattice strain and P-introducing on D-band center, the DOS of Ni@NiP-3 % with different ratio of P-introducing, which is donated as Ni@NiP-3 %-x (x represents the number of P atoms replace Ni atoms on the top layer), was calculated and results were shown in Fig. S21. It can be found that the D-band center of Ni@NiP-3 %-x shifts negatively with the increase in P-introducing amount. Therefore, tensile lattice strain is the key factor to raise D-band center of Ni@NiP-3 %. To sum up, the high catalytic activity of strained Ni@NiP to BOR ascribes to the energy difference decrease of the RDS due to the rise of D-band center caused by the tensile lattice strain.

3.4. Direct borohydride fuel cell performance

Ni@NiP, Pt/C, and Pd/C catalysts are separately used as the anode to further research the influences on OCV and performances of a fuel cell. Fig. 5a displays the polarization curves and power density curves of DBFCs using different anode catalysts. When using Ni@NiP anode, the OCV of the DBFC reaches 1.92 V, while that is merely 1.79 V using the Pt/C anode. The higher OCV implies the poorer competition reaction due to the fact that OCV of DBFC is a mixed voltage with BOR and its competition reaction[6]. Thus, this also demonstrates the higher catalytic selectivity of the Ni@NiP to BOR than that of Pt/C. Moreover, employing the Ni@NiP anode, DBFC shows a peak power density of 474 mW cm^{-2}, which is 2.5 times and twice as high as that with the Pt/C (187 mW cm^{-2}) and Pd/C (240 mW cm^{-2}) anodes, respectively. In

addition, Fig. 5b and Table S4 compares the performances of DBFCs using the Ni@NiP anode with those using noble-metal-based (Pd[2,10, 11,28,69] and Au[32,70–72]), and other Ni-based[9,13,14,21] anodes. It can be seen that the peak power density of the DBFC with the Ni@NiP anode is much higher than most with noble metal-based anodes, and is comparable to that with the state-of-the-art metal-based anode. The long-term stability of the DBFC with the Ni@NiP anode was further evaluated by chronopotentiometry. As shown in Fig. 5c, the DBFC can maintain a stable working voltage for more than 40 h. During DBFC operation, the slight decrease of working voltage is attributed to the consumption of BH$_4^-$ in anolyte and H$_2$O$_2$ in catholyte, which can be recovered by replacing electrolyte. As shown in Fig. 5d, assembled by Ni@NiP anode and Pt/C cathode, the unit DBFC can light up a series of LED lights with a rated voltage of approximately 1.8 V, which indicates promising application prospects.

4. Conclusion

In summary, a facile fabrication strategy of strained Ni-based catalyst has presented and the relationship of electrocatalytic performances and the lattice strain studied in details. The Ni-based catalyst has a core-shell structure consisting of amorphous NiP shell and crystalline Ni core. And the Ni lattice is expanded to generate tensile lattice strain due to P introduction into the shell. The Ni@NiP-1.2 with 3% tensile lattice strain, which has the best performance, shows a high current density of 255 mA cm^{-2}, a low Tafel slope of 149.3 mV dec^{-1}, low activation energy of 8.1 kJ mol^{-1}, and a large transfer electron number of 7.2. Moreover, its intrinsic activity is 6.3 mA cm$_{Cat.}^{-2}$, much superior to other reported catalysts to BOR. With Ni@NiP anode, DBFC provides the peak power density of 474 mW cm^{-2} and the OCV of 1.92 V, much higher than those with commercial Pt/C, Pd/C, and most reported anodes. DFT calculation reveals that the formation of B* intermediate is the RDS and the catalytic activity to BOR is effectively improved by the formation energy reduction of B* on strained Ni@NiP surface due to the rise of D-band center caused by tensile lattice strain. This work provides ideas not only for the development of advanced electrocatalysts for borohydride
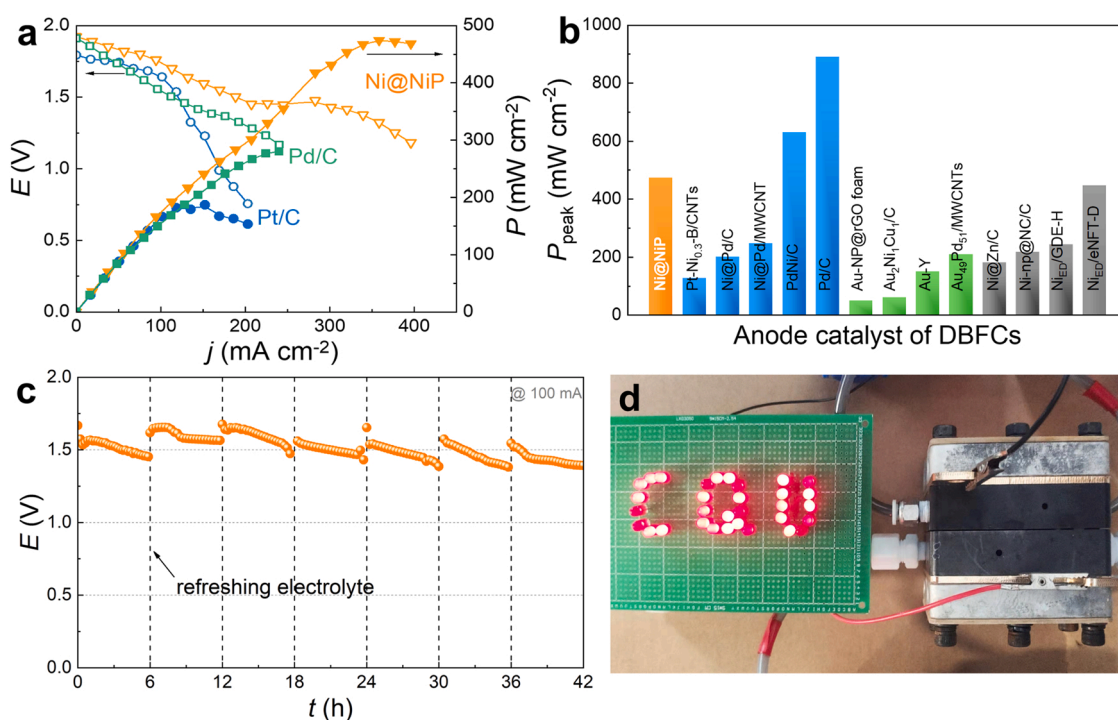
Fig. 5. (a) Polarization curves and power density curves of the DBFC with the Ni@NiP anode, commercial Pt/C, and Pd/C anodes, respectively; (b) performance comparison of DBFCs; (c) long-term stability test and (d) practical application of the DBFC with the Ni@NiP anode.

oxidation and the design of low-cost DBFC anodes with outstanding performance, but also improvement performance of other related transition-metal-based electrocatalysts.

CRediT authorship contribution statement

Bihao Hu: Conceptualization, Investigation, Formal analysis, Writing – original draft, Validation. **Yuxin Xie:** Methodology, Formal analysis, Writing – original draft, Validation. **Ying Yang:** Validation, Writing – review & editing. **Jiazhi Meng:** Validation. **Jinliang Cai:** Validation. **Changguo Chen:** Resources, Supervision. **Danmei Yu:** Resources, Writing – review & editing, Supervision, Project administration. **Xiaoyuan Zhou:** Resources, Supervision, Funding acquisition.

Declaration of Competing Interest

The authors declare that they have no known competing financial interests or personal relationships that could have appeared to influence the work reported in this paper.

Data Availability

Data will be made available on request.

Acknowledgment

Appendix A. Supporting information

Supplementary data associated with this article can be found in the online version at doi:10.1016/j.apcatb.2022.122257.

References

[1] B.P. Setzler, Z. Zhuang, J.A. Wittkopf, Y. Yan, Activity targets for nanostructured platinum-group-metal-free catalysts in hydroxide exchange membrane fuel cells, Nat. Nanotechnol. 11 (2016) 1020–1025, https://doi.org/10.1038/nnano.2016.265.

[2] Z. Wang, S. Sankarasubramanian, V. Ramani, Reactant-transport engineering approach to high-power direct borohydride fuel cells, Cell Rep. Phys. Sci. 1 (2020), 100084, https://doi.org/10.1016/j.xcrp.2020.100084.

[3] Z. Wang, J. Parrondo, C. He, S. Sankarasubramanian, V. Ramani, Efficient pH-gradient-enabled microscale bipolar interfaces in direct borohydride fuel cells, Nat. Energy 4 (2019) 281–289, https://doi.org/10.1038/s41560-019-0330-5.

[4] I. Merino-Jiménez, C. Ponce De León, A.A. Shah, F.C. Walsh, Developments in direct borohydride fuel cells and remaining challenges, J. Power Sources 219 (2012) 339–357, https://doi.org/10.1016/j.jpowsour.2012.06.091.

[5] J.H. Wee, Which type of fuel cell is more competitive for portable application: Direct methanol fuel cells or direct borohydride fuel cells, J. Power Sources 161 (2006) 1–10, https://doi.org/10.1016/j.jpowsour.2006.07.032.

[6] Z. Wang, J. Parrondo, C. He, S. Sankarasubramanian, V. Ramani, Efficient pH-gradient-enabled microscale bipolar interfaces in direct borohydride fuel cells, Nat. Energy 4 (2019) 281–289, https://doi.org/10.1038/s41560-019-0330-5.

[7] C.P. de León, F.C. Walsh, A. Rose, J.B. Lakeman, D.J. Browning, R.W. Reeve, A direct borohydride-acid peroxide fuel cell, J. Power Sources 164 (2007) 441–448, https://doi.org/10.1016/j.jpowsour.2006.10.069.

[8] P.Y. Olu, N. Job, M. Chatenet, Evaluation of anode (electro)catalytic materials for the direct borohydride fuel cell: Methods and benchmarks, J. Power Sources 327 (2016) 235–257, https://doi.org/10.1016/j.jpowsour.2016.07.041.

[9] A.G. Oshchepkov, G. Braesch, S. Ould-Amara, G. Rostamikia, G. Maranzana, A. Bonnefont, V. Papaefthimiou, M.J. Janik, M. Chatenet, E.R. Savinova, Nickel metal nanoparticles as anode electrocatalysts for highly efficient direct borohydride fuel cells, ACS Catal. 9 (2019) 8520–8528, https://doi.org/10.1021/acscatal.9b01616.

[10] S. Saha, P. Gayen, Z. Wang, R.J. Dixit, K. Sharma, S. Basu, V.K. Ramani, Development of bimetallic PdNi electrocatalysts toward mitigation of catalyst poisoning in direct borohydride fuel cells, ACS Catal. 11 (2021) 8417–8430, https://doi.org/10.1021/acscatal.1c00768.

[11] Y. Zhou, S. Li, Y. Chen, Y. Liu, The high utilization of fuel in direct borohydride fuel cells with a PdNix-B/carbon nanotubes-catalysed anode, J. Power Sources 351 (2017) 79–85, https://doi.org/10.1016/j.jpowsour.2017.03.056.

[12] R.C.P. Oliveira, J. Milikić, E. Daş, A.B. Yurtcan, D.M.F. Santos, B. Šljukić, Platinum/polypyrrole-carbon electrocatalysts for direct borohydride-peroxide fuel cells, Appl. Catal. B 238 (2018) 454–464, https://doi.org/10.1016/j.apcatb.2018.06.057.

[13] B. Hu, J. Yu, J. Meng, C. Xu, J. Cai, B. Zhang, Y. Liu, D. Yu, X. Zhou, C. Chen, Porous Ni-Cu alloy dendrite anode catalysts with high activity and selectivity for direct borohydride fuel cells, ACS Appl. Mater. Interfaces 14 (2022) 3910–3918, https://doi.org/10.1021/acsami.1c15671.

[14] B. Hu, P. Chen, C. Xu, J. Meng, J. Cai, Y. Yang, B. Zhang, D. Yu, X. Zhou, C. Chen, Hierarchical leaf-shaped Ni@Zn bimetallic catalyst with high stability and selectivity for borohydride oxidation, Appl. Catal. B 307 (2022), 121183, https://doi.org/10.1016/j.apcatb.2022.121183.

[15] P.Y. Olu, A. Bonnefont, M. Rouhet, S. Bozdech, N. Job, M. Chatenet, E. Savinova, Insights into the potential dependence of the borohydride electrooxidation reaction mechanism on platinum nanoparticles supported on ordered carbon nanomaterials, Electrochim. Acta 179 (2015) 637–646, https://doi.org/10.1016/j.electacta.2015.02.158.

[16] G. Rostamikia, R.J. Patel, I. Merino-Jimenez, M. Hickner, M.J. Janik, Electrocatalyst design for direct borohydride oxidation guided by first principles, J. Phys. Chem. C 121 (2017) 2872–2881, https://doi.org/10.1021/acs.jpcc.6b12159.

[17] S. Saha, P. Gayen, Z. Wang, R.J. Dixit, K. Sharma, S. Basu, V.K. Ramani, Development of bimetallic PdNi electrocatalysts toward mitigation of catalyst poisoning in direct borohydride fuel cells, ACS Catal. 11 (2021) 8417–8430, https://doi.org/10.1021/acscatal.1c00768.

[18] M.C.S. Escaño, R.L. Arevalo, E. Gyenge, H. Kasai, Electrocatalysis of borohydride oxidation: A review of density functional theory approach combined with experimental validation, J. Phys. Condens. Matter 26 (2014), https://doi.org/10.1088/0953-8984/26/35/353001.

[19] B. Hu, J. Yu, J. Meng, C. Xu, J. Cai, B. Zhang, Y. Liu, D. Yu, X. Zhou, C. Chen, Porous Ni-Cu alloy dendrite anode catalysts with high activity and selectivity for direct borohydride fuel cells, ACS Appl. Mater. Interfaces 14 (2022) 3910–3918, https://doi.org/10.1021/acsami.1c15671.

[20] J. Yu, B. Hu, C. Xu, J. Meng, S. Yang, Y. Li, X. Zhou, Y. Liu, D. Yu, C. Chen, Ni-P amorphous alloy efficient electrocatalyst with hierarchical structure toward borohydride oxidation, Dalton Trans. (2021), https://doi.org/10.1039/d1dt01031j.

[21] G. Braesch, Z. Wang, S. Sankarasubramanian, A.G. Oshchepkov, A. Bonnefont, E.R. Savinova, V. Ramani, M. Chatenet, A high performance direct borohydride fuel cell using bipolar interfaces and noble metal-free Ni-based anodes, J. Mater. Chem. A Mater. 8 (2020) 20543–20552, https://doi.org/10.1039/d0ta06405j.

[22] W. Ni, T. Wang, P.A. Schouwink, Y.C. Chuang, H.M. Chen, X. Hu, Efficient Hydrogen Oxidation Catalyzed by Strain-Engineered Nickel Nanoparticles, Angew. Chem. - Int. Ed. 59 (2020) 10797–10801, https://doi.org/10.1002/anie.201916314.

[23] M. Gong, D.Y. Wang, C.C. Chen, B.J. Hwang, H. Dai, A mini review on nickel-based electrocatalysts for alkaline hydrogen evolution reaction, Nano Res. 9 (2016) 28–46, https://doi.org/10.1007/s12274-015-0965-x.

[24] T. Wang, M. Wang, H. Yang, M. Xu, C. Zuo, K. Feng, M. Xie, J. Deng, J. Zhong, W. Zhou, T. Cheng, Y. Li, Weakening hydrogen adsorption on nickel via interstitial nitrogen doping promotes bifunctional hydrogen electrocatalysis in alkaline solution, Energy Environ. Sci. 12 (2019) 3522–3529, https://doi.org/10.1039/c9ee01743g.

[25] E. Gyenge, M. Atwan, D. Northwood, Electrocatalysis of borohydride oxidation on colloidal Pt and Pt-alloys (Pt-Ir, Pt-Ni, and Pt-Au) and application for direct borohydride fuel cell anodes, J. Electrochem. Soc. 153 (2006) A150, https://doi.org/10.1149/1.2131831.

[26] R. Mahmoodi, M.G. Hosseini, H. Rasouli, Enhancement of output power density and performance of direct borohydride-hydrogen peroxide fuel cell using Ni-Pd core-shell nanoparticles on polymeric composite supports (rGO-PANI) as novel electrocatalysts, Appl. Catal. B 251 (2019) 37–48, https://doi.org/10.1016/j.apcatb.2019.03.064.

[27] M.G. Hosseini, R. Mahmoodi, Ni@M (M = Pt, Pd and Ru) core@shell nanoparticles on a Vulcan XC-72R support with superior catalytic activity toward borohydride oxidation: electrochemical and fuel cell studies, New J. Chem. 41 (2017) 13408–13417, https://doi.org/10.1039/c7nj02585h.

[28] M.G. Hosseini, R. Mahmoodi, Improvement of energy conversion efficiency and power generation in direct borohydride-hydrogen peroxide fuel cell: the effect of Ni-M core-shell nanoparticles (M = Pt, Pd, Ru)/Multiwalled Carbon Nanotubes on the cell performance, J. Power Sources 370 (2017) 87–97, https://doi.org/10.1016/j.jpowsour.2017.10.017.

[29] M.G. Hosseini, V. Daneshvari-Esfahlan, S. Wolf, V. Hacker, Novel bimetallic Pd-X (X = Ni, Co) nanoparticles assembled on N-Doped reduced graphene oxide as an anode catalyst for highly efficient direct sodium borohydride-hydrogen peroxide fuel cells, ACS Appl. Energy Mater. (2021) (2021), https://doi.org/10.1021/acsaem.1c00876.

[30] X. Ma, K. Ye, G. Wang, M. Duan, K. Cheng, G. Wang, D. Cao, Facile fabrication of gold coated nickel nanoarrays and its excellent catalytic performance towards sodium borohydride electro-oxidation, Appl. Surf. Sci. 414 (2017) 353–360, https://doi.org/10.1016/j.apsusc.2017.04.104.

[31] D. Duan, J. Liang, H. Liu, X. You, H. Wei, G. Wei, S. Liu, The effective carbon supported core-shell structure of Ni@Au catalysts for electro-oxidation of

borohydride, Int J. Hydrog. Energy 40 (2015) 488–500, https://doi.org/10.1016/j.ijhydene.2014.10.101.

[32] D. Duan, X. Yin, Q. Wang, S. Liu, Y. Wang, Performance evaluation of borohydride electrooxidation reaction with ternary alloy Au–Ni–Cu/C catalysts, J. Appl. Electrochem. 48 (2018) 835–847, https://doi.org/10.1007/s10800-018-1208-0.

[33] Y. e Duan, S. Li, Q. Tan, Y. Chen, K. Zou, X. Dai, M. Bayati, B.B. Xu, L. Dala, T. X. Liu, Cobalt nickel boride nanocomposite as high-performance anode catalyst for direct borohydride fuel cell, Int. J. Hydrog. Energy 46 (2021) 15471–15481, https://doi.org/10.1016/j.ijhydene.2021.02.064.

[34] Z. Xia, S. Guo, Strain engineering of metal-based nanomaterials for energy electrocatalysis, Chem. Soc. Rev. 48 (2019) 3265–3278, https://doi.org/10.1039/c8cs00846a.

[35] A. Nilsson, L.G.M. Pettersson, B. Hammer, T. Bligaard, C.H. Christensen, J. K. Nørskov, The electronic structure effect in heterogeneous catalysis, Catal. Lett. 100 (2005) 111–114, https://doi.org/10.1007/s10562-004-3434-9.

[36] P. Strasser, S. Koh, T. Anniyev, J. Greeley, K. More, C. Yu, Z. Liu, S. Kaya, D. Nordlund, H. Ogasawara, M.F. Toney, A. Nilsson, Lattice-strain control of the activity in dealloyed core-shell fuel cell catalysts, Nat. Chem. 2 (2010) 454–460, https://doi.org/10.1038/nchem.623.

[37] T. He, W. Wang, F. Shi, X. Yang, X. Li, J. Wu, Y. Yin, M. Jin, Mastering the surface strain of platinum catalysts for efficient electrocatalysis, Nature 598 (2021) 76–81, https://doi.org/10.1038/s41586-021-03870-z.

[38] C. Cui, L. Gan, M. Heggen, S. Rudi, P. Strasser, Compositional segregation in shaped Pt alloy nanoparticles and their structural behaviour during electrocatalysis, Nat. Mater. 12 (2013) 765–771, https://doi.org/10.1038/nmat3668.

[39] Q. Jia, W. Liang, M.K. Bates, P. Mani, W. Lee, S. Mukerjee, Activity descriptor identification for oxygen reduction on platinum-based bimetallic nanoparticles: In situ observation of the linear composition-strain-activity relationship, ACS Nano 9 (2015) 387–400, https://doi.org/10.1021/nn506721f.

[40] H. Huang, H. Jia, Z. Liu, P. Gao, J. Zhao, Z. Luo, J. Yang, J. Zeng, Understanding of strain effects in the electrochemical reduction of CO2: using Pd nanostructures as an ideal platform, Angew. Chem. - Int. Ed. 56 (2017) 3594–3598, https://doi.org/10.1002/anie.201612617.

[41] S.E. Temmel, E. Fabbri, D. Pergolesi, T. Lippert, T.J. Schmidt, Investigating the role of strain toward the oxygen reduction activity on model thin film Pt catalysts, ACS Catal. 6 (2016) 7566–7576, https://doi.org/10.1021/acscatal.6b01836.

[42] L. Wang, Z. Zeng, W. Gao, T. Maxson, D. Raciti, M. Giroux, X. Pan, C. Wang, J. Greeley, Tunable intrinsic strain in two-dimensional transition metal electrocatalysts, Science 363 (2019) (1979) 870–874, https://doi.org/10.1126/scienceaat8051.

[43] J.M. Montejano-Carrizales, F. Aguilera-Granja, J.L. Morán-López, Direct enumeration of the geometrical characteristics of clusters, Nanostruct. Mater. 8 (1997) 269–287, https://doi.org/10.1016/S0965-9773(97)00168-2.

[44] J.M. Montejano-Carrizales, J.L. Morán-López, Geometrical characteristics of compact nanoclusters, Nanostruct. Mater. 1 (1992) 397–409, https://doi.org/10.1016/0965-9773(92)90090-K.

[45] S.A.S. Machado, L.A. Avaca, The hydrogen evolution reaction on nickel surfaces stabilized by H-absorption, Electrochim. Acta 39 (1994) 1385–1391, https://doi.org/10.1016/0013-4686(94)E0003-I.

[46] Z. Zhuang, S.A. Giles, J. Zheng, G.R. Jenness, S. Caratzoulas, D.G. Vlachos, Y. Yan, Nickel supported on nitrogen-doped carbon nanotubes as hydrogen oxidation reaction catalyst in alkaline electrolyte, Nat. Commun. 7 (2016) 1–8, https://doi.org/10.1038/ncomms10141.

[47] W. Ni, T. Wang, F. Héroguel, A. Krammer, S. Lee, L. Yao, A. Schüler, J. S. Luterbacher, Y. Yan, X. Hu, An efficient nickel hydrogen oxidation catalyst for hydroxide exchange membrane fuel cells, Nat. Mater. (2022), https://doi.org/10.1038/s41563-022-01221-5.

[48] B. Li, C. Song, X. Huang, K. Ye, K. Cheng, K. Zhu, J. Yan, D. Cao, G. Wang, A novel anode for direct borohydride-hydrogen peroxide fuel cell: Au nanoparticles decorated 3D self-supported reduced graphene oxide foam, ACS Sustain. Chem. Eng. 7 (2019) 11129–11137, https://doi.org/10.1021/acssuschemeng.9b00192.

[49] G. Braesch, A. Bonnefont, V. Martin, E.R. Savinova, M. Chatenet, Borohydride oxidation reaction mechanisms and poisoning effects on Au, Pt and Pd bulk electrodes: from model (low) to direct borohydride fuel cell operating (high) concentrations, Electrochim. Acta 273 (2018) 483–494, https://doi.org/10.1016/j.electacta.2018.04.068.

[50] G. Kresse, J. Hafner, Ab initio molecular dynamics for liquid metals, Phys. Rev. B 47 (1993) 558–561, https://doi.org/10.1103/PhysRevB.47.558.

[51] D. Joubert, From ultrasoft pseudopotentials to the projector augmented-wave method, Phys. Rev. B Condens Matter Mater. Phys. 59 (1999) 1758–1775, https://doi.org/10.1103/PhysRevB.59.1758.

[52] J.P. Perdew, K. Burke, M. Ernzerhof, Generalized Gradient Approximation Made Simple (vol 77, pg 3865, 1996), Phys Rev Lett. 78 (1997) 1396–1396.

[53] J.P. Perdew, A. Ruzsinszky, G.I. Csonka, O.A. Vydrov, G.E. Scuseria, L. A. Constantin, X. Zhou, K. Burke, Restoring the density-gradient expansion for exchange in solids and surfaces, Phys. Rev. Lett. 100 (2008) 1–4, https://doi.org/10.1103/PhysRevLett.100.136406.

[54] R.A. Vargas-Hernández, Bayesian optimization for calibrating and selecting hybrid-density functional models, J. Phys. Chem. A 124 (2020) 4053–4061, https://doi.org/10.1021/acs.jpca.0c01375.

[55] K. Hu, M. Wu, S. Hinokuma, T. Ohto, M. Wakisaka, J.I. Fujita, Y. Ito, Boosting electrochemical water splitting: via ternary NiMoCo hybrid nanowire arrays, J. Mater. Chem. A Mater. 7 (2019) 2156–2164, https://doi.org/10.1039/c8ta11250a.

[56] J. Yu, B. Hu, C. Xu, J. Meng, S. Yang, Y. Li, X. Zhou, Y. Liu, D. Yu, C. Chen, An efficient Ni-P amorphous alloy electrocatalyst with a hierarchical structure toward borohydride oxidation, Dalton Trans. 50 (2021) 10168–10179, https://doi.org/10.1039/d1dt01031j.

[57] H. Tianou, W. Wang, X. Yang, Z. Cao, Q. Kuang, Z. Wang, Z. Shan, M. Jin, Y. Yin, Inflating hollow nanocrystals through a repeated Kirkendall cavitation process, Nat. Commun. 8 (2017) 1–8, https://doi.org/10.1038/s41467-017-01258-0.

[58] A. Roustila, C. Severac, J. Chêne, A. Percheron-Guégan, Hydrogen effects on the electronic and microstructural properties of Ce, Ni, and CeNi2 intermetallic compound, Surf. Sci. 311 (1994) 33–44, https://doi.org/10.1016/0039-6028(94)90478-2.

[59] Z. Huang, Z. Chen, Z. Chen, C. Lv, H. Meng, C. Zhang, Ni12P5 nanoparticles as an efficient catalyst for hydrogen generation via electrolysis and photoelectrolysis, ACS Nano 8 (2014) 8121–8129, https://doi.org/10.1021/nn5022204.

[60] J. Zhang, X. Cao, M. Guo, H. Wang, M. Saunders, Y. Xiang, S.P. Jiang, S. Lu, Unique Ni crystalline Core/Ni phosphide amorphous shell heterostructured electrocatalyst for hydrazine oxidation reaction of fuel cells, ACS Appl. Mater. Interfaces 11 (2019) 19048–19055, https://doi.org/10.1021/acsami.9b00878.

[61] B. Hammer, J.K. Norskov, Theoretical surface science and catalysis - Calculations and concepts, in: B.C. Gates, H. Knozinger (Eds.), ADVANCES IN CATALYSIS, VOL 45: IMPACT OF SURFACE SCIENCE ON CATALYSIS, Aalborg Univ, Inst Phys, DK-9220 Aalborg, Denmark, 2000: pp. 71–129 WE-Science Citation Index Expanded (SCI-.

[62] R. Chattot, O. Le Bacq, V. Beermann, S. Kühl, J. Herranz, S. Henning, L. Kühn, T. Asset, L. Guétaz, G. Renou, J. Drnec, P. Bordet, A. Pasturel, A. Eychmüller, T. J. Schmidt, P. Strasser, L. Dubau, F. Maillard, Surface distortion as a unifying concept and descriptor in oxygen reduction reaction electrocatalysis, Nat. Mater. 17 (2018) 827–833, https://doi.org/10.1038/s41563-018-0133-2.

[63] L. Dubau, J. Nelayah, T. Asset, R. Chattot, F. Maillard, Implementing structural disorder as a promising direction for improving the stability of PtNi/C nanoparticles, ACS Catal. 7 (2017) 3072–3081, https://doi.org/10.1021/acscatal.7b00410.

[64] R. Chattot, T. Asset, P. Bordet, J. Drnec, L. Dubau, F. Maillard, Beyond strain and ligand effects: Microstrain-induced enhancement of the oxygen reduction reaction kinetics on various PtNi/C nanostructures, ACS Catal. 7 (2017) 398–408, https://doi.org/10.1021/acscatal.6b02356.

[65] A.G. Oshchepkov, G. Braesch, G. Rostamikia, A. Bonnefont, M.J. Janik, M. Chatenet, E.R. Savinova, Insights into the borohydride electrooxidation reaction on metallic nickel from operando FTIRS, on-line DEMS and DFT, Electro Acta 389 (2021), 138721, https://doi.org/10.1016/j.electacta.2021.138721.

[66] Y. Zhao, C. Fang, Y. Fang, F. Zhu, H. Liu, H. Ge, Hydrogen generation mechanism of BH4− spontaneous hydrolysis: A sight from ab initio calculation, Int. J. Hydrog. Energy 41 (2016) 22668–22676, https://doi.org/10.1016/j.ijhydene.2016.10.057.

[67] J. Andrieux, U.B. Demirci, J. Hannauer, C. Gervais, C. Goutaudier, P. Miele, Spontaneous hydrolysis of sodium borohydride in harsh conditions, Int. J. Hydrog. Energy 36 (2011) 224–233, https://doi.org/10.1016/j.ijhydene.2010.10.055.

[68] B.R. Karimadom, D. Meyerstein, H. Kornweitz, Calculating the adsorption energy of a charged adsorbent in a periodic metallic system-The case of BH4-hydrolysis on the Ag(111) surface, Phys. Chem. Chem. Phys. 23 (2021) 25667–25678, https://doi.org/10.1039/d1cp03895h.

[69] M.G. Hosseini, R. Mahmoodi, Ni@M (M = Pt, Pd and Ru) core@shell nanoparticles on a Vulcan XC-72R support with superior catalytic activity toward borohydride oxidation: electrochemical and fuel cell studies, New J. Chem. 41 (2017) 13408–13417, https://doi.org/10.1039/c7nj02585h.

[70] B. Li, C. Song, X. Huang, K. Ye, K. Cheng, K. Zhu, J. Yan, D. Cao, G. Wang, A novel anode for direct borohydride-hydrogen peroxide fuel cell: Au nanoparticles decorated 3D self-supported reduced graphene oxide foam, ACS Sustain. Chem. Eng. 7 (2019) 11129–11137, https://doi.org/10.1021/acssuschemeng.9b00192.

[71] T.H. Oh, Gold-based bimetallic electrocatalysts supported on multiwalled carbon nanotubes for direct borohydride–hydrogen peroxide fuel cell, Renew. Energy 163 (2021) 930–938, https://doi.org/10.1016/j.renene.2020.09.028.

[72] G. Backović, J. Milikić, S. de Negri, A. Saccone, B. Šljukić, D.M.F. Santos, Enhanced borohydride oxidation kinetics at gold-rare earth alloys, J. Alloy. Compd. 857 (2021), https://doi.org/10.1016/j.jallcom.2020.158273.